Chemistry Journals
Analytical, Inorganic, Organic, Physical, Materials Science

Numerical study of valence band states evolution in $Al_xGa_{1-x}As$ [111] QDs systems

Mikhail Lazarev [Corresp. 1]

[1] Faculty of computer science, Laboratory of Methods for Big Data Analysis, HSE University, Moscow, Russia

Corresponding Author: Mikhail Lazarev
Email address: mvlazarev@hse.ru

Quantum Dots (QDs) are very attractive nanostructures from an application point of view due to their unique optical properties. Optical properties and Valence Band (VB) states character was numerically investigated from the effect of nanostructure geometry and composition. Numerical simulation was carried out using Luttinger–Kohn model adapted to the particular use case of QDs in inverted pyramids. We present the source code of the 4-band Luttinger–Kohn model that can be used to model AlGaAs or InGaAs nanostructures. Here we focus on the optical properties study of GaAs/AlGaAs [111] QDs and Quantum Dot Molecules (QDMs). We examine the dependence of Ground State (GS) optical properties on their structural parameters and predict optimal parameters of the QD/QDM systems to achieve the dynamic control of GS polarization by the applied electric field.

1 # Numerical study of Valence Band states evolution in $Al_xGa_{1-x}As$ [111] QDs

2 # systems

3 *M. Lazarev[1]*

4 *[1] Faculty of Computer Science, Laboratory of Methods for Big Data Analysis, HSE University,*

5 *Russia*

6 Corresponding Author:
7 Mikhail Lazarev[1]
8 Pokrovsky Blvd, 11, Moscow, 109028
9 Email address: mvlazarev@hse.ru

10 ## Abstract

11 Quantum Dots (QDs) represent a class of nanostructures that are highly attractive from an
12 application point of view due to their unique optical properties. Optical properties and Valence
13 Band (VB) states character was numerically investigated from the effect of nanostructure geometry
14 and composition. Numerical simulation was carried out using the Luttinger–Kohn model adapted
15 to the particular use case of QDs in inverted pyramids. Here, we focus on the optical properties
16 study of GaAs/AlGaAs [111] QDs and Quantum Dot Molecules (QDMs). We examine the
17 dependence of Ground State (GS) optical properties on their structural parameters and predict
18 optimal parameters of the QD/QDM systems to achieve the tunable control of GS polarization by
19 the applied electric field. We present the source code of the 4-band Luttinger–Kohn model that
20 can be used as a comprehensive tool for simulating AlGaAs or InGaAs nanostructures.

21 ## 1. Introduction

22 Low-dimensional nanostructures have unique optical properties influenced by geometry and
23 composition. These properties have led to their diverse applications, ranging from photovoltaics
24 (Barnham et al., 2002), light-emitting diodes (LEDs) (Nakamura et al., 1995), to laser technologies
25 (Alferov, 2001), and so on (Levine, 1993). Dimensionality plays a curtail role in light-matter
26 interaction and the behavior of charge carriers, thereby influencing their optical characteristics. In
27 Quantum Wells (QWs), light emission happens due to the recombination of electrons with heavy
28 holes (Rau, B., P. Waltereit, O. Brandt, M. Ramsteiner, K. H. Ploog, J. Puls, 2000) in contrast to
29 Quantum Wires (QWRs), where recombination involves both heavy and light holes (Vouilloz et
30 al., 1997). Thus, nanostructure dimensionality impacts on emitted light polarization. QDs have a
31 complex spectral structure where carrier states can be heavy and light with high energy splitting.
32 Their ability to emit single photons positions them as potential integral components in the
33 emerging field of integrated quantum photonic circuits (Davanco et al., 2017)(Dietrich et al.,
34 2016)(Söllner et al., 2015).

35 Previous studies have established that the character of holes (heavy or light) in the Valence Band
36 (VB) of various nanostructures can be modulated by the structural design and material composition
37 of QDs (He et al., 2007)(Wang et al., 2008)(Zhu et al., 2007). Additionally, several methodologies
38 have been identified for achieving dynamic control over the optical properties of QDs. These
39 include the application of external electromagnetic fields (Fry et al., 2000)(Bennett et al., 2010)
40 and strain (Martín-, 2018). Several groups have demonstrated electrically driven position control
41 of QD in photonic crystals (Carter et al., 2013) and cavity and polarization control in micropillar
42 cavities (Rakher et al., 2008)(Reitzenstein & Forchel, 2010). Further, the modification of emission
43 wavelengths through the application of external stress has been successfully implemented(Zhang
44 et al., 2014). The study of dynamic control over QD band structure is fundamental for novel
45 functional materials and devices in a wide range of applications.

46 QD band structure can be calculated using multiple methodologies, ranging from ab initio
47 approaches (Reimann & Manninen, 2002)(Kohn & Sham, 1965) to empirical pseudopotential
48 method (Mäder & Zunger, 1994) and (Boykin et al., 2007). While these methods offer detailed
49 insights, their extensive computational demands often render them impractical for simulating
50 heterostructure electronic structures. On the other hand, the **kp** methods are widely applied to
51 describe III–V semiconductor heterostructures optical properties. Application of 4-band and 6-
52 band Luttinger–Kohn **kp** models for (111)-oriented systems were introduced in (Kelsall RW,
53 Taylor RI, Wood AC, 1989)(Majewski, Stadele & Vogi, 1997) (Marquardt, O'Reilly & Schulz,
54 2014)(Kajikawa, 1999). There are even higher dimensional models, 8-band (Tomić, Sunderland
55 & Bush, 2006)(Andrzejewski et al., 2010), 10-band (Gladysiewicz et al., 2013), and even 30-band
56 models(Song et al., 2020), although they lack publicly available source code for verification. A
57 larger model gives more accurate predictions, allowing us to consider more accurate effects like a
58 decrease of optical gain for InGaAs/GaAs QWs with an increase in the hydrostatic pressure
59 (Gladysiewicz, Kudrawiec & Wartak, 2014) (10-band vs 8-band). However, the needed accuracy
60 depends on the application and experimental setup. Here, to describe nanostructure VB properties,
61 we use a relatively simple 4-band **kp** model implemented in the code (Lazarev M. & Karlsson F.,
62 2022), which agrees with experimental data obtained in previous studies. The 4-band **kp** model is
63 a fast solution that describes the VB structure well. The detailed model description is presented in
64 Section 2 of this article. Here, we theoretically study the transition process between Light and
65 Heavy holes like VB ground state (GS) characters in QDs of different geometries. We use the same
66 modeling approach as in (Zhu et al., 2009)(Troncale et al., 2007)(Lazarev, Rudra & Kapon, 2023).

67 In this study, we focus on Quantum Dots (QDs) grown within inverted pyramid structures, as
68 previously explored (Karlsson et al., 2006)(Zhu et al., 2010). Nanostructures in inverted pyramids
69 are well studied experimentally and demonstrate the ability to control the structure composition
70 and geometry with high precision during material deposition. The MOVPE growth technique
71 allows the growing of all possible varieties of nanostructures by controlling heterostructure
72 composition along the growth direction. The schematic illustrations are presented in Figure 1. Each
73 nanostructure in Figure 1 represents a nanostructure type that has been experimentally fabricated

74   and reported in the literature; for example QWRs (Figure 1 a) (Zhu et al., 2006), QDs (Figure 1 b)
75   (Zhu et al., 2007), tailored QDs (Lazarev, Rudra & Kapon, 2023)(Szeszko et al., 2012)(Zhu et al.,
76   2006) (Figure 1 e), QDMs (Zhu et al., 2009) (Figure 1 d) Dot-in-Dot (DiD) (Troncale et al., 2007)
77   (Figure 1 c). Different colors correspond to Al content in the structure in Figure 1 (a), schematically
78   presented QWR (symmetry center) in an inverted pyramid. Due to the physical processes of
79   nanostructure growth, QWR formation is always accompanied by the formation of side
80   nanostructures QWs. In Figure 1 (a), such side nanostructures are colored green for Vertical QW
81   and blue for Vicinal QWs colors. Summarily to QWR, the QD also forms its side nanostructures,
82   Lateral QWRs. Thus, QD formation in QWR is presented in Figure 1 (b). Tailoring of Al content
83   during the growth allows to realize all possible nanostructures in solid form. In this study, we
84   consider the central QWR region. In earlier work (Zhu et al., 2007), pyramidal $Al_xGa_{1-x}As$ QDs
85   with heights of 10-100 nm were realized, and as it was reported by changing the QD size, it's
86   possible to control polarization properties. In (Zhu et al., 2007), little attention was paid to the
87   related VB states structure.

88

89   *Figure 1. Schematic illustration of different kinds of AlGaAs nanostructures embedded in inverted*
90   *pyramids. (a) "Long" quantum wire laterally bounded by "vertical" QWs, (b) Quantum Dot, and*
91   *(c) QD-in-QD heterostructure. (d) QDM of two coupled QDs. (e) Tailored potential QWR/QD.*
92   *The color codes scale the Al mole fraction in the different parties of the heterostructures.*

93   Achievement of dynamic control over light polarization emitted by the nanostructures in the
94   inverted pyramid is an area of significant interest. Dynamic control of the GS emission polarization
95   of quantum Dot in Dot (DiD) pyramidal nanostructure was proposed in (Troncale, Karlsson &
96   Kapon, 2010). However, the study used geometrical assumptions of the nanostructure that do not
97   match experimental results, and the source code is not available. In (V. Troncale, 2010)
98   polarization optical properties of DiD in magnetic field study were reported, but polarization
99   switching requires high magnetic field intensities and hence is not feasible for applications.

100   In this paper, we theoretically study VB GSs evolution in pyramidal QD/QDM systems from the
101   geometry and material composition that forms the potential profile. The paper is divided into a few
102   parts; in Section 2 introduces the simulation method (subsection 2.1) and outlines the structural
103   design approximations employed (subsection 2.2). Section 3 is dedicated to simulation results; in
104   subsection 3.1, we present single QD simulation results of GS VB evolution from its length and
105   electric field. In subsection 3.2, we study the evolution of the QDM system. In section 4, we
106   conclude your findings. The Appendix contains the 4x4 Luttinger Hamiltonian derivation used in
107   this study.

108   **2. Method**

109   **2.1 Theory**

110 Here, we introduce the model with assumptions we used and implemented in the code (Lazarev
111 M. & Karlsson F., 2022). Portions of this text here and below were previously published as part
112 of a thesis (Lazarev, 2019). As a basis, we start with the Kane Hamiltonian (Kane, 1957):

113 $H = H^{k \cdot p} + H_{SO}$, where $H^{k \cdot p} = \left[\dfrac{p^2}{2m_0} + V(r) \right] + \left[\dfrac{h}{m_0} k \cdot p + \dfrac{h^2 k^2}{2m_0} \right]$ and $H_{SO} = \dfrac{h}{4m_0^2 c^2} \sigma \cdot [\nabla V \times p]$

114 thus, the Schrödinger equation looks like:

115
$$\left(\left[\frac{p^2}{2m_0} + V(r) \right] + \left[\frac{h}{m_0} k \cdot p + \frac{h^2 k^2}{2m_0} \right] + \frac{h}{4m_0^2 c^2} \sigma \cdot [\nabla V \times (p + hk)] \right) u_k^{(n)}(r) = \varepsilon_k^{(n)} u_k^{(n)}(r) \qquad (1)$$

116 Where σ are Paul matrixes, ∇V the gradient of atomic mean field potential, $u_k^{(n)}(r)$ the Bloch
117 waves, and m_0 is the electron mass. Our model works with Hamiltonian (1) and solves it in a 4-
118 band (S and P orbitals) approximation. To achieve more accurate results and consider the influence
119 of other bands, Löwdin perturbation theory [27] was implied. See the supplementary material in
120 the Appendix for more details.

121 To each pair of electron and hole corresponds exciton energy and definer as follows:

122 $E_X = E_g + E_{cb} + E_{vb} - E_{Coulomb}^{e-h}$ where E_{cb}, E_{vb} are the state energies in CB and VB, and $E_{Coulomb}^{e-h}$
123 is Coulomb interaction energy. These values depend on QD geometry and material composition.
124 Usually, in small QDs, confinement energy is strong compared to the Coulomb interaction. The
125 Coulomb interaction in the case of strong confinement can be considered as a perturbation
126 (Warburton et al., 1998). The perturbation to the Hamiltonian is then written as:

127
$$E_{Coulomb}^{e-h} = \iint \psi_{cb} \psi_{vb} \frac{e^2}{4\pi\varepsilon_0 \varepsilon |r_{cb} - r_{vb}|} \psi_{cb}^* \psi_{vb}^* dr_{cb} dr_{vb} \qquad (2)$$

128 where ψ_{vb}, ψ_{cb} are the valence and conduction band wavefunctions, r_{cb}, r_{vb} the electron and hole
129 positions.

130 Observed light intensity and polarization dependence proportional to dipole moment matrix
131 element (Löwdin, 1951):

132
$$I_{eh} = \sum_{S_z = \pm\frac{1}{2}} \left| \sum_{J_z = \pm\frac{3}{2}, \pm\frac{1}{2}} \left\langle \phi_e^{S_z}(r) \middle| \phi_h^{J_z}(r) \right\rangle \left\langle u_e^{S_z} \middle| e \, p \middle| u_h^{J_z} \right\rangle \right|^2 \qquad (3)$$

133 Where e is polarization, p is the momentum operator, and u is Bloch wavefunction.

134   The final expression for polarization dependence in the case of orthogonal LH and HH
135   wavefunctions along and perpendicular z direction is:

$$136 \quad I_z \propto \left(\frac{4}{3} \langle \varphi_e | \varphi_{LH} \rangle^2 \right) \quad I_{xy} \propto \left(\langle \varphi_e | \varphi_{HH} \rangle^2 + \frac{1}{3} \langle \varphi_e | \varphi_{LH} \rangle^2 \right) \tag{4}$$

137   Spectral measurements often use the degree of linear polarization (DOLP) value. Here we define

138   DOLP as $DOLP = \frac{I_z - I_{xy}}{I_z + I_{xy}}$. Thus $DOLP = -1$ corresponds to transition HH wavefunction (WF)

139   part and $DOLP = 0.6$ LH WF part.

2.2 Modeling of structure composition

141   In our analysis, the parameters defining material distribution and geometry are derived from
142   previous research (Zhu et al., 2006). The design of the structure's special parameters is based on a
143   simplified model of the "effective" Al-content resulting from the capillarity-driven Al-Ga
144   segregation at the sharp wedges of the. The ratio between "effective" and "nominal" Al content:

$$145 \quad x_{eff} = \frac{x}{x + K(1-x)} \tag{5}$$

146   where x is the nominal (bulk) Al concentration. For different arias of the pyramidal nanostructure
147   K parameter is unique, so $K=8.9$ for the central QWR region and $K=2.1$ for side QWs [24]. Since
148   the x_{eff} in an Al content, by definition, is associated with the QWR spectral line (Zhu et al., 2006),
149   it leads to an overestimation of actual Al by the blue shift of ~30meV (or ~2% Al content). The
150   overestimation is constant in all points of QWR; thus, it does not affect CB or VB structure. This
151   statement is consistent with experimental results. Effective Al content permits calculating the
152   bandgap profile of the corresponding components of the 3D pyramidal heterostructure. In this
153   paper, we implement an additional assumption: due to similar Al content to the bulk, we neglect
154   LQWs regions (blue color in Figure 1(a)), assuming Al content to be the same as in the bulk. More
155   geometry details and the ratio of material distribution are also well described in previous studies
156   (Zhu et al., 2006) (Lazarev, Rudra & Kapon, 2023). The bandgap dependence over Al content in
157   GaAs is known from the literature (Vurgaftman, Meyer & Ram-Mohan, 2001):

$$158 \quad E_g \left(Al_x Ga_{1-x} As \right) = (1-x) E_g \left(GaAs \right) + x E_g \left(AlAs \right) - x(1-x) C \tag{6}$$

159   where C is the bowing parameter, $E_g(GaAs) = 1.519\,\text{eV}$ and $E_g(AlAs) = 3.1\,\text{eV}$ (low-
160   temperature values). According to (6), each 1% of Al content gives ~15 meV to the band gap. The
161   band gap offsets ratio between the CB and VB was taken as ΔCB/ ΔVB ~67/33(Kopf et al.,
162   1992)(Langbein, Gislason & Hvam, 1996).

163   In our computational framework, Al$_x$Ga$_{1-x}$As [111] nanostructures within inverted pyramids are

164   the primary focus, although the code is versatile enough to accommodate any 3D structure
165   specified by the user. The option to add *In* content to GaAs and correspondent Hamiltonian is also
166   implemented. It is important to note that $In_xGa_{1-x}As$ compound is a material with internal strain,
167   and the Hamiltonian presented above must be modified. While our current discussion does not
168   delve into the strain-modified Hamiltonian, this feature is also incorporated into the code. The
169   numerical solution of the Hamiltonian was performed by the finite difference method.

170   An example of the model structure geometry is presented in Figure 2, which is a 10 nm thick GaAs
171   QD embedded in AlGaAs barriers. The modeled area is 40x40 nm size which is enough to make
172   sure that border conditions (infinite barriers) do not have an effect on the exciton structure in the
173   area of interest. The calculation grid parameter is chosen as 0.1 nm for all simulation results
174   presented in this paper. The diameter of the QD/QWR cylinders is kept at 18 nm. Figure 2 b
175   illustrates the Al distribution in the ZX plane. To reiterate key parameters, the effective Al content
176   within the core cylinder of the QD is approximately 2.8%, and in the vertical barrier cylinders, it
177   stands at about ~7.2% (for 40% nominal Al content).

178

179

180   *Figure 2. (a) 3D isosurface of Al content (x=0.4) in a simulated 10 nm thick GaAs QD*
181   *nanostructure. (b) Z-X cut of the simulated nanostructure showing Al content distribution.*

182   This methodology was successfully applied to analyze experimental results. In the paper (Lazarev,
183   Rudra & Kapon, 2023), the impact of valence band mixing and spectrum of confined states on the
184   polarization of emitted light from QDs with tailored potential was explored as a function of
185   confinement potential shape that allows it to carefully examine the effect of nanostructure
186   dimensionality on nanostructure emission properties.

187   **3. Results and discussion**

188   **3.1 LH and HH states evolution in QD**

189   Figure 3 (a) presents the calculated energies of the lowest CB and VB (Figure 3 (b)) states as a
190   function of QD thickness *t*, exclusive of Coulomb interaction effects. The height *t* of the QD
191   cylinder (the QD "thickness") is varied between 8 to 20 nm (see inset in Fig. 3(a)). The effective
192   Al content in the core cylinder of the QD is ~2.7% (for 20% nominal Al content. In the vertical
193   barrier cylinders, it is ~7.2% (for 40% nominal Al content), which is illustrated in Figure 3 (e) as
194   a dark and light region in the vertical wire region (pyramid center). The LH (blue color) and HH
195   (red color) states cross in energy for QD thickness $t \sim 13$ (see Figure 3 (b)). Remarkably, this
196   transition also takes places in the VB mixing characteristic (Figure 3 (d)), where at the crossover
197   point, the HH and the LH WF portions are the same for the first two VB states. For $t < 13$ nm, the

198   ground state is HH-like, with smaller t the structure behaves in his respect as a "thin" QD. For
199   $t > 13$ nm, the ground state is LH-like, with larger t the structure behaves as a "QWR" or
200   elongated QD. These results suggest the searching area to choose QD parameters for achieving a
201   structure at the border between HH and LH behavior of the VB ground state. To achieve more
202   accurate results the Coulomb interaction must be considered.

203   The calculated polarization-resolved optical spectra of this QD structure are shown in Figure 3 (c)
204   for various thicknesses t; red and blue curves correspond to linear polarization normal and parallel
205   to the growth direction. Figure 3 (e) schematically presents light polarization axes with respect to
206   the nanostructure. Line broadening of 2 meV was applied, and Coulomb interaction was taken into
207   account as a perturbation. This set of spectra shows how the GS transition gradually changes its
208   character from LH to HH with a reduction of QD thickness. Interestingly, the switching from HH
209   to LH – like lowest energy state occurs near $t = 14$ nm (as in Figure 3(b)), which is different on
210   1nm from switching simulated without coulomb interaction.

211

212   *Figure 3. (a) Calculated dependence of energy of first CB state from QD thickness. (b) Calculated*
213   *dependence of energy of first two VB states from QD thickness. Blue corresponds to LH transitions,*
214   *and red corresponds to HH transitions. (c) Calculated absorption spectra of t=8 nm, 10 nm, 12*
215   *nm, 14 nm, 16 nm, 18 nm, 20 nm QD thickness. Different colors correspond to different*
216   *polarizations. Blue is emission polarized in the Z direction and red in the XY plane. (d) Calculated*
217   *wavefunction portions of the first two VB states from QD thickness. The red color is the state with*
218   *HH, and another one by the blue color with LH major parts. (e) Schematic illustration of QD in*
219   *an inverted pyramid with the indication of parallel and perpendicular light polarization.*

220   In a range of $t \sim 14$ nm, the QD GS transition changes its polarization with the "switching" of the
221   VB ground state character from LH to HH. Since, around this point, small variations in the
222   confinement potential can yield such GS character "switching", such QD can serve as a base for
223   achieving the desired tunable transition using an electric field. Here, we analyze the effect of an
224   electric field on such "equilibrium": QD structure.

225   To illustrate the effect of an electric field, we consider the same QD structure discussed above with
226   fixed QD thickness at $t = 14$ nm. The confined CB and VB states are then computed by adding an
227   electric field E oriented in the growth direction z. From the experimental point of view, considering
228   the structure size of $L < 1 \mu m$ the voltage magnitude at $T = 10 K$ that can be applied is about 3V,
229   it gives us a feasible range of electric field simulation up to $E_{max} = 30 \, [\text{kV/cm}]$.

230   Figure 4 (a) shows the calculated optical spectra of the QD structure for an electric field of
231   amplitude $E = 20$ [kV/cm] oriented along the growth direction. We would like to highlight two
232   significant differences compared to the spectrum for $E = 0$. First, the absorption edge is red-shifted

233 due to a quantum confined Stark effect (Fry et al., 2000). Secondly, the lowest energy transition
234 line with nearly equal H and V light intensity components develops for $E > 0$ into a richer structure
235 with characteristic polarization features. This is illustrated by DOLP spectrum, which shows an
236 HH-like feature at low energies instead of $DOLP \sim 0$ for $E = 0$. The reason is that the electric
237 field changes the QD potential profile in such a way that the lowest VB state becomes HH-like,
238 and the Stark shifts are different for the different VB states. Thus, applying an electric field can
239 tune the QD structure to change the polarization state of light emitted by the QD ground states.
240 The impact of the electric field on the lowest transition state energy is displayed on the right panel
241 of Figure 4. The spectral lines near 1.595eV in Figure 4 are related to the first CB and first two
242 VB transitions. Note that the polarization is determined by the part (LH or HH) of the VB
243 wavefunction that best overlaps with the CB state.

244

245 *Figure 4. QD (t=14 nm), subject to an electric field E=20 kV/cm, applied in the z direction. Left*
246 *panel: (a) Calculated optical spectra taking into account Coulomb interaction and 2 meV*
247 *broadening. (b) DOLP spectra. Right panel: schematic presentation of QD in an inverted pyramid*
248 *with electric contact and wavefunctions isosurfaces of the GS CB state and parts of two lowest VB*
249 *states that overlap with GS CB: green – electron; red – HH; blue - LH.*

250 **3.2 QDM Polarization control by barrier adjustment**

251

252 *Figure 5. Schematic illustration of two QDs systems (QD molecule) embedded in an inverted*
253 *pyramid. The color illustrates the Al mole fraction in the different parties of the heterostructures.*

254 QDM systems contain many parameters that affect QDs coupling strength, and thus, system's
255 optical properties, the main geometrical parameters, are illustrated schematically in Figure 5. For
256 example, here, we show the effect of barrier height on the polarization switching of the QDM GS
257 emission. Figure 6 presents the dependence of the lowest CB and VB states on Al content (in
258 'nominal' values) in the outer barrier (nominal Al content in QD core: 20%; in external barriers:
259 40%, QD thickness $t = 7$ nm; barrier thickness $d = 5$ nm). The GS of the CB increases with
260 increasing Al content as the potential energy of the barrier increases. The VB states dependence is
261 more complex: in between the two extreme barrier heights, the VB GS changes its character from
262 LH- to HH- like with increasing Al content (see Figure 6 b).

263

264 *Figure 6. (a) Calculated energy dependence of the first CB state versus the QDM barrier*
265 *composition (in "nominal" values of Al content). (b) Calculated energy of the first two VB states*

266 *from QD barrier composition. The blue line corresponds to LH transitions, and the red*
267 *corresponds to HH transitions. The inset is a schematic of the QDM core part.*

268 Figure 7 (a) presents a comprehensive summary of the calculated optical spectra, considering
269 Coulomb interaction as a perturbation and a line broadening of 2 meV. The lowest energy
270 transition is mainly LH-like for low barriers and becomes degenerate with the HH-like one at
271 ~40% Al. The spectra show the evolution of the HH and LH transition lines, their crossing when
272 Al content becomes ~40%, and at 50%, the complete change of the GS to HH one. Figure 7 (b)
273 shows the spectral positions of the GS and the first excited transition versus the barrier Al content,
274 indicating the VB character (red color for HH, blue for LH). Figure 7 (c) shows the VB mixing
275 dependence on the barrier height. In summary, the common trend for all structures is that at certain
276 inner QDs coupling regimes (from strong to low), the GS transition changes between LH to HH-
277 like. As a consequence, the emission polarization of the GS also changes. This figure illustrates
278 the two regimes of behavior, with two different GS transition types and polarization of emitted
279 light. The QDM system at the intermediate point where the HH and LH states are almost
280 degenerate opens an opportunity to tune the GS emission character by applying an external electric
281 field due to the sensitivity of such structure.

282

283 *Figure 7. (a) Calculated absorption spectra of the QDM for different heights of the barrier (in*
284 *"nominal" values Al content). Lines corresponding to HH-like and LH-like transitions are*
285 *indicated. (b) Calculated energies of the lowest energy transitions (a) versus QDM thickness*
286 *barrier height. Different colors correspond to different transition types: the red line between CB*
287 *and HH transition and the blue line between CB and LH transition. (c) Major wavefunction parts*
288 *of the first two VB states dependence, HH - red and LH - blue.*

289 Next, we consider the effect of an external electric field in a QDM with the following structural
290 parameters: QD cores of 20% Al content and thickness $t = 7$ nm each, QD external barriers of 40%
291 Al content, QD inner barrier thickness $d = 5$ nm, and 35% Al content. Figure 8 shows the
292 simulation results of the system without an external electric field ($E = 0$). Figure 8 (a) presents the
293 calculated optical spectra, and Figure 8 (b) the corresponding DOLP spectra. In this configuration,
294 the GS LH and HH transition is almost at the same energy, with a more complex structure of the
295 excited states transitions. The right panel of Figure 8 shows a side view of the lowest CB and VB
296 states WFs isosurfaces.

297

298 *Figure 8. QDM structure (see text for parameters) without an electric field. Left panel: (a)*
299 *Calculated absorption spectra taking into account Coulomb interaction and 2 meV broadening.*
300 *(b) DOLP spectra. Right panel: wavefunctions isosurfaces of the GS CB state and parts of two*
301 *lowest VB states that overlap with GS CB: green – electron; red – HH; blue - LH.*

302 For the same QDM structure, the other potential asymmetry induced by an external electric field
303 of $E = 0.9$ [kV/cm] aligned in the growth direction dramatically changes the optical spectra and
304 WFs shapes (Figure 9). As in the case of the single QD with the applied electric field, the
305 polarization of the GS transition and its energy change. In contrast to the case $E = 0$, the lowest
306 energy transition now has $DOLP = -0.6$ instead of $DOLP = 0.5$ to its more important HH character
307 of the VB state involved. As usual, the electric field pushes the CB and VB WFs in the opposite
308 direction for a Stark effect. This also leads to a reduction in the transition strength due to the
309 smaller WF overlaps.

310

311 *Figure 9. QDM structure (see text for parameters) subject to an electric field E=0.9 kV/cm, applied*
312 *in the +z direction. Left panel: (a) Calculated absorption spectra taking into account Coulomb*
313 *interaction and 2 meV broadening. (b) DOLP spectra. Right panel: wavefunctions isosurfaces of*
314 *the GS CB state and parts of two lowest VB states that overlap with GS CB: green – electron; red*
315 *– HH; blue - LH.*

316 The case of two-QDs molecule can be extended to N QDs (QDSLs), which leads us to the
317 formation of minibands (Sugaya et al., 2010), as was also shown in the case of QW superlattices
318 (R. Dingle and etc., 1975). Such systems can also be realized experimentally in inverted pyramids
319 as a vertically aligned coupled QD array. In QDSLs, the barriers height and width are crucial
320 parameters that define the coupling strength between the QDs. In such systems with modulated
321 internal potential in a low coupling regime, GS HH WFs can have as large as LH WF in QDs with
322 flat potential. However, the corresponding emission will have a different polarization. The
323 consequence of low coupling is that a "forest" of close-spaced optical transition lines appears.
324 Under the application of an electric field, the excited CB and VB WFs overlap due to tunneling to
325 neighbor QDs, while the first CB and VB states are separate and do not overlap (Lazarev, 2019).
326 From an experimental point of view, it's hard to fabricate and analyze the VB structure of N QDs
327 due to structural complexity, optical line merging, and non-linear effects during the nanostructure
328 growth.

329 **4. Conclusion**

330 The sensitivity of VB state structure to the environment of QD and QDM makes them as promising
331 candidates for polarization-controlled single photon sources. A number of QDs were simulated by 4-
332 band Luttinger–Kohn **kp** model with QDs thickness from 8 nm and 23 nm in length. The
333 "equilibrium" point where LH and HH have the same energy positions was identified in QDs
334 approximately 14 nm in length. Applying an electric field along the QD allows us to control the VB
335 structure so that VB GS character becomes HH or LH, which can be observed experimentally by
336 measuring DOLP. Modulating the coupling strength in QDM by the potential variations in the barrier
337 between the QDs we study QDM sensitivity of optical properties to its structural parameters. We show
338 that QDMs are more sensitive to an external electric field than single QDs and demonstrate how it

339 affects QDM absorption spectra. This knowledge will be helpful for the construction of future
340 polarization-switching devices.

341 The model source code (Lazarev M. & Karlsson F., 2022) may be helpful for similar studies or
342 educational purposes. The code is available on Github: *https://github.com/Mikelazarev/Low-*
343 *dimensional-band-structure-model-*

5. Acknowledgment

345 My acknowledgments go to Prof. Fredrik Karlsson for providing numerical codes. Also, I would
346 like to thank Prof. Eli Kapon for the useful discussions.

347
348

6. References

350

351 Alferov ZI. 2001. Nobel lecture: The double heterostructure concept and its applications in
352   physics, electronics, and technology. *Reviews of Modern Physics* 73:767–782. DOI:
353   10.1103/RevModPhys.73.767.

354 Andrzejewski J, Sęk. G, O'Reilly E, Fiore A, Misiewicz J. 2010. Eight-band k.p calculations of
355   the composition contrast effect on the linear polarization properties of columnar quantum
356   dots. *Journal of Applied Physics* 107:0–12. DOI: 10.1063/1.3346552.

357 Barnham KWJ, Ballard I, Connolly JP, Ekins-Daukes NJ, Kluftinger BG, Nelson J, Rohr C.
358   2002. Quantum well solar cells. *Physica E: Low-Dimensional Systems and Nanostructures*
359   14:27–36. DOI: 10.1016/S1386-9477(02)00356-9.

360 Bennett AJ, Pooley MA, Stevenson RM, Ward MB, Patel RB, De La Giroday AB, Sköd N,
361   Farrer I, Nicoll CA, Ritchie DA, Shields AJ. 2010. Electric-field-induced coherent coupling
362   of the exciton states in a single quantum dot. *Nature Physics* 6:947–950. DOI:
363   10.1038/nphys1780.

364 Boykin TB, Kharche N, Klimeck G, Korkusinski M. 2007. Approximate bandstructures of
365   semiconductor alloys from tight-binding supercell calculations. *Journal of Physics
366   Condensed Matter* 19. DOI: 10.1088/0953-8984/19/3/036203.

367 Carter SG, Sweeney TM, Kim M, Kim CS, Solenov D, Economou SE, Reinecke TL, Yang L,
368   Bracker AS, Gammon D. 2013. Quantum control of a spin qubit coupled to a photonic
369   crystal cavity. *Nature Photonics* 7:329–334. DOI: 10.1038/nphoton.2013.41.

370 Davanco M, Liu J, Sapienza L, Zhang C-Z, De JV, Cardoso M, Verma V, Mirin R, Nam SW,
371   Liu L, Srinivasan K. 2017. Heterogeneous integration for on-chip quantum photonic circuits
372   with single quantum dot devices. *Nature communications* 8:889. DOI: 10.1038/s41467-017-
373   00987-6.

374 Dietrich CP, Fiore A, Thompson MG, Kamp M, Ofling S. 2016. GaAs integrated quantum
375   photonics: Towards compact and multi-functional quantum photonic integrated circuits.
376   *Laser & photonics reviews* 10:870–894.

377 Fry PW, Itskevich IE, Mowbray DJ, Skolnick MS, Finley JJ, Barker JA, O'Reilly EP, Wilson
378   LR, Larkin IA, Maksym PA, Hopkinson M, Al-Khafaji M, David JPR, Cullis AG, Hill G,
379   Clark JC. 2000. Inverted Electron-Hole Alignment in InAs-GaAs Self-Assembled Quantum
380   Dots. *Physical Review Letters* 84:733–736. DOI: 10.1103/PhysRevLett.84.733.

381 Gladysiewicz M, Kudrawiec R, Miloszewski JM, Weetman P, Misiewicz J, Wartak MS. 2013.
382   Band structure and the optical gain of GaInNAs/GaAs quantum wells modeled within 10-
383   band and 8-band kp model. *Journal of Applied Physics* 113. DOI: 10.1063/1.4790568.

384 Gladysiewicz M, Kudrawiec R, Wartak MS. 2014. Theoretical studies of optical gain tuning by
385   hydrostatic pressure in GaInNAs/GaAs quantum wells. *Journal of Applied Physics*
386   115:033515. DOI: 10.1063/1.4862230.

387 He J, Krenner HJ, Pryor C, Zhang JP, Wu Y, Allen DG, Morris CM, Sherwin MS, Petroff PM.
388   2007. Growth, structural, and optical properties of self-assembled (In,Ga)As quantum posts
389   on GaAs. *Nano Letters* 7:802–806. DOI: 10.1021/nl070132r.

390 Kajikawa Y. 1999. Optical anisotropy of (11l)-oriented strained quantum-wells calculated with
391   the effect of the spin-orbit split-off band. *Journal of Applied Physics* 86:5663–5677. DOI:
392   10.1063/1.371577.

393 Kane EO. 1957. Band structure of indium antimonide. *Journal of Physics and Chemistry of*
394   *Solids* 1:249–261. DOI: 10.1016/0022-3697(57)90013-6.

395 Karlsson KF, Troncale V, Oberli DY, Malko A, Pelucchi E, Rudra A, Kapon E. 2006. Optical
396   polarization anisotropy and hole states in pyramidal quantum dots. *Applied Physics Letters*
397   89. DOI: 10.1063/1.2402241.

398 Kelsall RW, Taylor RI, Wood AC AR. 1989. Hole transport and relaxation in the valence bands
399   of GaAs/AlAs quantum well. *Superlattices and Microstructures* 5:207–211. DOI:
400   https://doi.org/10.1016/0749-6036(89)90285-1.

401 Kohn W, Sham LJ. 1965. Self-Consistent Equations Including Exchange and Correlation Effects.
402   *Physical review* 140. DOI: 10.1103/PhysRev.140.A1133.

403 Kopf RF, Herman MH, Schnoes ML, Perley AP, Livescu G, Ohring M. 1992. Band offset
404   determination in analog graded parabolic and triangular quantum wells of GaAs/AlGaAs
405   and GaInAs/AlInAs. *Journal of Applied Physics* 71:5004–5011. DOI: 10.1063/1.350600.

406 Langbein W, Gislason H, Hvam JM. 1996. Optimization of the confinement energy of quantum-
407   wire states in T-shaped GaAs/Al(x)Ga(1-x)As structures. *Phys. Rev. B* 54:14595–14603.
408   DOI: 10.1103/PhysRevB.54.14595.

409 Lazarev M. 2019. Tailored-Potential Semiconductor Quantum Nanostructures Grown in Inverted

410   Pyramids. *PhD Theses, Lausanne, EPFL*. DOI: https://doi.org/10.5075/epfl-thesis-9461.

411   Lazarev M., Karlsson F. 2022. Low-dimensional semiconductor band structure model based on
412   4-band approximation k.p theory. DOI: 10.5281/ZENODO.7438050.

413   Lazarev M, Rudra A, Kapon E. 2023. Physical origins of optical anisotropy in quantum-confined
414   semiconductors: The roles of valence band mixing, transition broadening, and state filling.
415   *Journal of Applied Physics* 133. DOI: 10.1063/5.0131958.

416   Levine BF. 1993. Quantum-well infrared photodetectors. *Journal of Applied Physics* 74. DOI:
417   10.1063/1.354252.

418   Löwdin PO. 1951. A note on the quantum-mechanical perturbation theory. *The Journal of*
419   *Chemical Physics* 19:1396–1401. DOI: 10.1063/1.1748067.

420   Mäder KA, Zunger A. 1994. Empirical atomic pseudopotentials for AlAs/GaAs superlattices,
421   alloys, and nanostructures. *Physical Review B* 50:17393–17405. DOI:
422   10.1103/PhysRevB.50.17393.

423   Majewski JA, Stadele M, Vogi P. 1997. Electronic structure of biaxially-strained wurtzite
424   crystals GaN and AlN. *Materials Research Society Symposium - Proceedings* 449:887–892.
425   DOI: 10.1557/proc-449-887.

426   Marquardt O, O'Reilly EP, Schulz S. 2014. Electronic properties of site-controlled (111)-
427   oriented zinc-blende InGaAs/GaAs quantum dots calculated using a symmetry-adapted k · p
428   Hamiltonian. *Journal of Physics Condensed Matter* 26. DOI: 10.1088/0953-
429   8984/26/3/035303.

430   Martín- J. 2018. Strain-tuning of the optical properties of semiconductor nanomaterials by
431   integration onto piezoelectric actuators. *Semicond. Sci. Technol* 33. DOI: 10.1088/1361-
432   6641/aa9b53.

433   Nakamura S, Senoh M, Iwasa N, Nagahama SI. 1995. High-power InGaN single-quantum-well-
434   structure blue and violet light-emitting diodes. *Applied Physics Letters* 67:1868. DOI:
435   10.1063/1.114359.

436   R. Dingle and etc. 1975. Direct Observation of Superlattice Formation in a Semiconductor
437   Heterostructure. *Physical Review Letters* 34:1327–1330.

438   Rakher MT, Stoltz NG, Coldren LA, Petroff PM, Bouwmeester D. 2008. Polarization-switchable
439   single photon source using the Stark effect. *Applied Physics Letters* 93:2008–2010. DOI:
440   10.1063/1.2978396.

441   Rau, B., P. Waltereit, O. Brandt, M. Ramsteiner, K. H. Ploog, J. Puls FH. 2000. In-plane
442   polarization anisotropy of the spontaneous emission of M -plane GaN/(Al, Ga) N quantum
443   wells. *Applied Physics Letters* 77:3343–3345. DOI: 10.1063/1.1326846.

444   Reimann SM, Manninen M. 2002. Electronic structure of quantum dots. *Reviews of Modern*

445   *Physics* 74:1283–1342. DOI: 10.1103/RevModPhys.74.1283.

446   Reitzenstein S, Forchel A. 2010. Quantum dot micropillars. *Journal of Physics D: Applied*
447   *Physics* 43. DOI: 10.1088/0022-3727/43/3/033001.

448   Söllner I, Mahmoodian S, Hansen SL, Midolo L, Javadi A, Kiršanske G, Pregnolato T, El-Ella
449   H, Lee EH, Song JD, Stobbe S, Lodahl P. 2015. Deterministic photon-emitter coupling in
450   chiral photonic circuits. *Nature Nanotechnology* 10:775–778. DOI:
451   10.1038/nnano.2015.159.

452   Song Z, Fan W, Tan CS, Wang Q, Nam D, Zhang DH, Sun G. 2020. Corrigendum: Band
453   structure of Ge 1-x Sn x alloy: a full-zone 30-band kp model. *New Journal of Physics*
454   22:019502. DOI: 10.1088/1367-2630/ab306f.

455   Sugaya T, Amano T, Mori M, Niki S. 2010. Miniband formation in InGaAs quantum dot
456   superlattice. *Applied Physics Letters* 97:2010–2013. DOI: 10.1063/1.3470108.

457   Szeszko J, Belykh V V., Gallo P, Rudra A, Karlsson KF, Sibeldin NN, Kapon E. 2012. Exciton
458   confinement and trapping dynamics in double-graded-bandgap quantum nanowires. *Applied*
459   *Physics Letters* 100:0–4. DOI: 10.1063/1.4721660.

460   Tomić S, Sunderland AG, Bush IJ. 2006. Parallel multi-band k·p code for electronic structure of
461   zinc blend semiconductor quantum dots. *Journal of Materials Chemistry* 16:1963–1972.
462   DOI: 10.1039/b600701p.

463   Troncale V, Karlsson KF, Kapon E. 2010. Dynamic switching of hole character and single
464   photon polarization using the quantum confined Stark effect in quantum dot-in-dot
465   structures. *Nanotechnology* 21. DOI: 10.1088/0957-4484/21/28/285202.

466   Troncale V, Karlsson KF, Pelucchi E, Rudra A, Kapon E. 2007. Control of valence band states in
467   pyramidal quantum dot-in-dot semiconductor heterostructures. *Applied Physics Letters*
468   91:45–48. DOI: 10.1063/1.2820693.

469   V. Troncale. 2010. Tailored-Potential Pyramidal Quantum Dot Heterostructures. *PhD thesis,*
470   *EPFL* 4786. DOI: 10.5075/EPFL-THESIS-4786.

471   Vouilloz F, Oberli DY, Dupertuis MA, Gustafsson A, Reinhardt F, Kapon E. 1997. Polarization
472   anisotropy and valence band mixing in semiconductor Quantum wires. *Physical Review*
473   *Letters* 78:1580–1583. DOI: 10.1103/PhysRevLett.78.1580.

474   Vurgaftman I, Meyer JR, Ram-Mohan LR. 2001. Band parameters for III-V compound
475   semiconductors and their alloys. *Journal of Applied Physics* 89:5815–5875. DOI:
476   10.1063/1.1368156.

477   Wang L, Rastelli A, Kiravittaya S, Atkinson P, Ding F, Bof Bufon CC, Hermannstädter C,
478   Witzany M, Beirne GJ, Michler P, Schmidt OG. 2008. Towards deterministically controlled
479   InGaAs/GaAs lateral quantum dot molecules. *New Journal of Physics* 10. DOI:
480   10.1088/1367-2630/10/4/045010.

481 Warburton RJ, Miller BT, Dürr CS, Bödefeld C, Karrai K, Kotthaus JP, Medeiros-Ribeiro G,
482   Petroff PM, Huant S. 1998. Coulomb interactions in small charge-tunable quantum dots: A
483   simple model. *Physical Review B* 58:16221–16231. DOI: 10.1103/PhysRevB.58.16221.

484 Zhang J, Huo Y, Rastelli A, Zopf M, Hö B, Chen Y, Ding F, Schmidt OG. 2014. Single Photons
485   On-Demand from Light-Hole Excitons in Strain- Engineered Quantum Dots. *Nano Letters*.
486   DOI: 10.1021/nl5037512.

487 Zhu Q, Ganière JD, He ZB, Karlsson KF, Byszewski M, Pelucchi E, Rudra A, Kapon E. 2010.
488   Pyramidal GaAs/ Alz Ga1-z As quantum wire/dot systems with controlled heterostructure
489   potential. *Physical Review B - Condensed Matter and Materials Physics* 82:1–13. DOI:
490   10.1103/PhysRevB.82.165315.

491 Zhu Q, Karlsson FK, Byszewski M, Rudra A, Pelucchi E, He Z, Kapon E. 2009. Hybridization
492   of electron and hole states in semiconductor quantum-dot molecules. *Small* 5:329–335.
493   DOI: 10.1002/smll.200801214.

494 Zhu Q, Karlsson KF, Pelucchi E, Kapon E. 2007. Transition from two-dimensional to three-
495   dimensional quantum confinement in semiconductor quantum wires/quantum dots. *Nano
496   Letters* 7:2227–2233. DOI: 10.1021/nl0706650.

497 Zhu Q, Pelucchi E, Dalessi S, Leiter K, Dupertuis MA, Kapon E. 2006. Alloy segregation,
498   quantum confinement, and carrier capture in self-ordered pyramidal quantum wires. *Nano
499   Letters* 6:1036–1041. DOI: 10.1021/nl060066d.

500

Figure 1

Schematic illustration of different kinds of AlGaAs nanostructures embedded in inverted pyramids

Schematic illustration of different kinds of AlGaAs nanostructures embedded in inverted pyramids. (a) "Long" quantum wire (QWR) laterally bounded by "vertical" QWs, (b) Quantum Dot, and (c) QD-in-QD heterostructure. (d) QDM of two coupled QDs. (e) Tailored potential QWR/QD. The color codes scale the Al mole fraction in the different parties of the heterostructures.
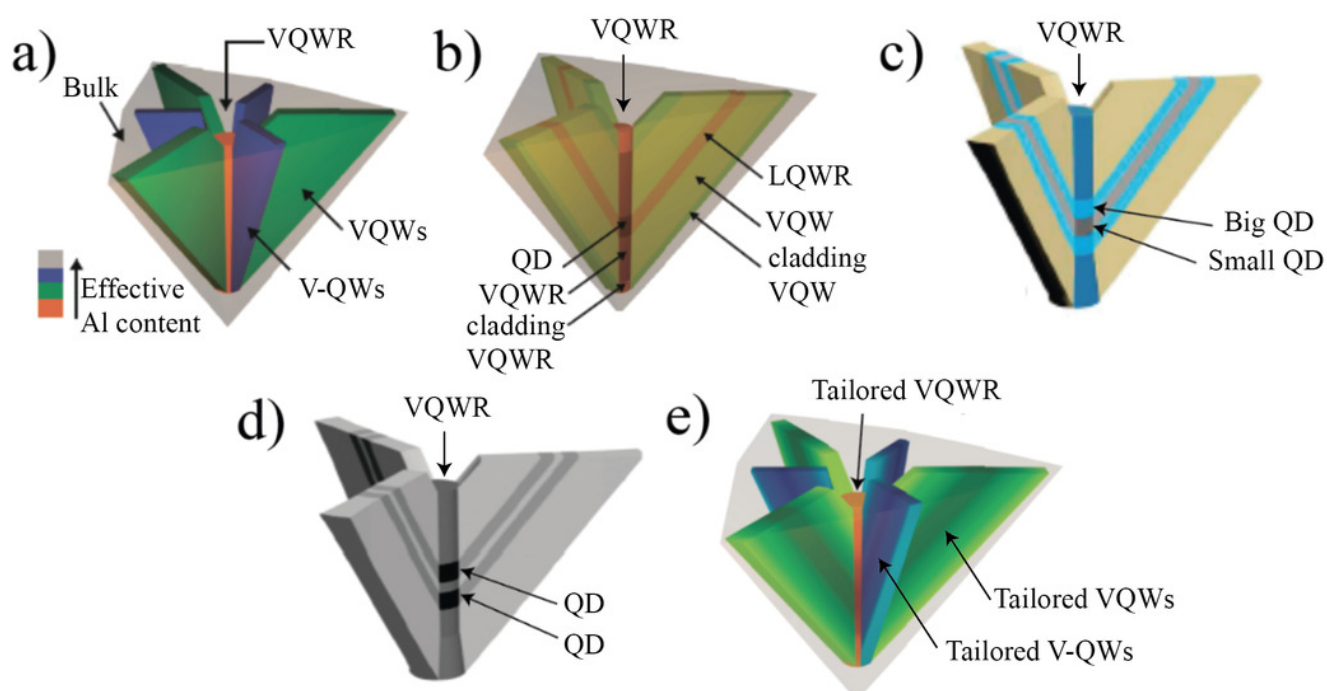
Figure 2

The example of the model structure geometry is presented, 10 nm thick GaAs QD embedded in AlGaAs barriers.

(a) 3D isosurface of Al content (x=0.4) in a simulated 10 nm thick GaAs QD nanostructure.

(b) Z-X cut of the simulated nanostructure showing Al content distribution.
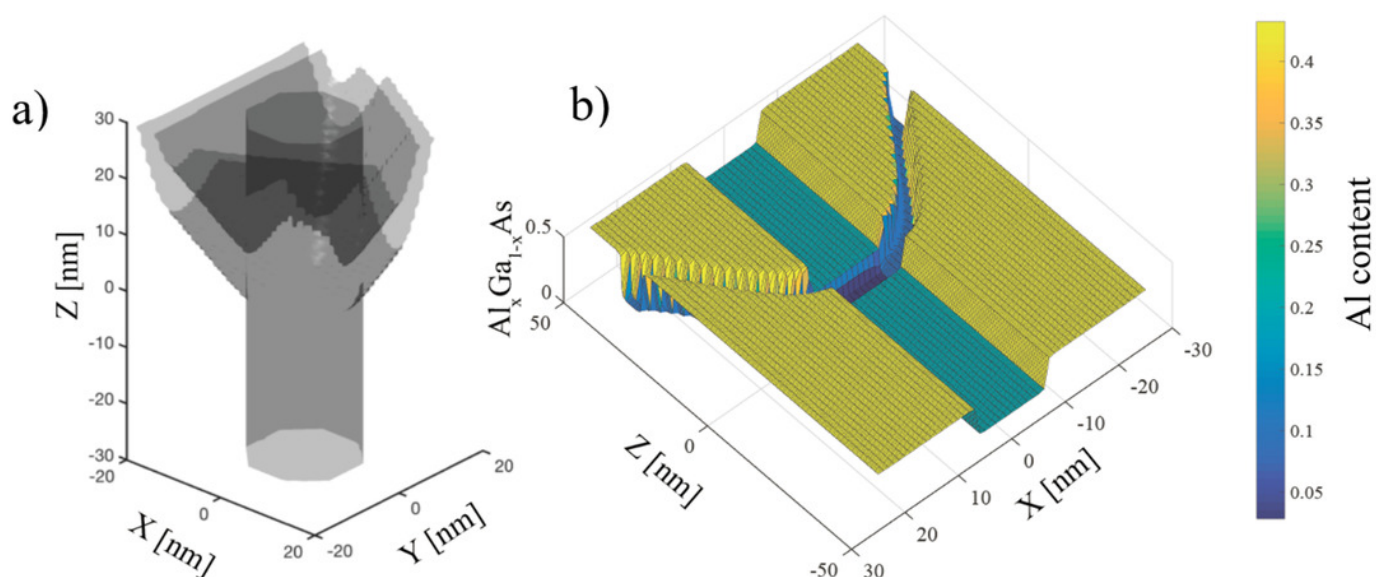
Figure 3

GS QD polarization-resolved optical spectra and VB structure for various thicknesses

(a) Calculated dependence of energy of first CB state from QD thickness. (b) Calculated dependence of energy of first two VB states from QD thickness. Blue color corresponds to LH transitions, and red color to HH transitions. (c) Calculated absorption spectra of t=8 nm, 10 nm, 12 nm, 14 nm, 16 nm, 18 nm, 20 nm QD thickness. Different colors correspond to different polarizations. Blue is emission polarized in the Z direction and red in the XY plane. (d) Calculated wavefunction portions of the first two VB states from QD thickness. The red color is the state with HH, and another one by the blue color with LH major parts. (e) Schematic illustration of QD in an inverted pyramid with the indication of parallel and perpendicular light polarization.
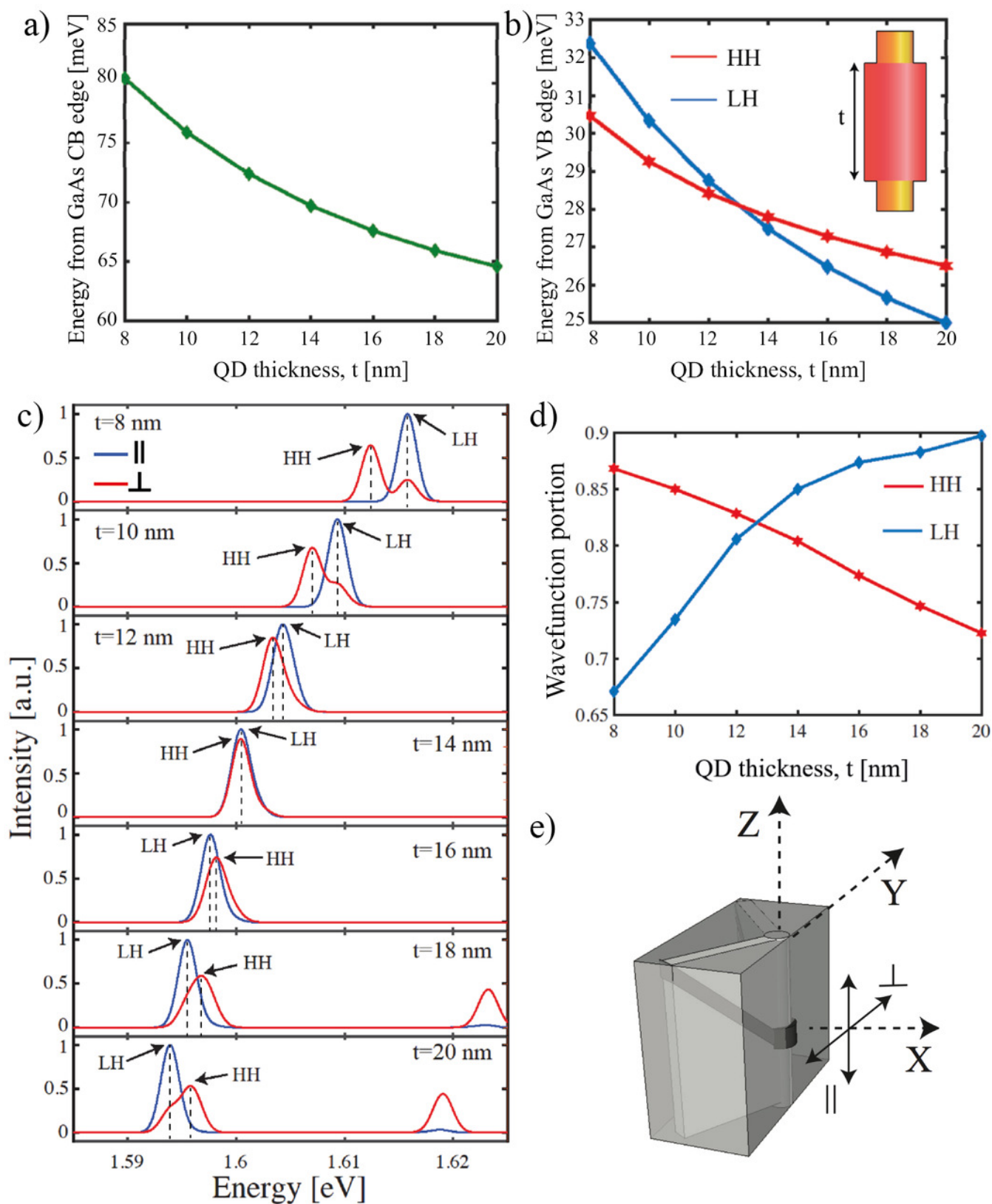
Figure 4

QD (t=14 nm), subject to an electric field E=20000 V/cm

QD (t=14 nm), subject to an electric field E=20000 V/cm, applied in the z direction. Left panel: (a) Calculated optical spectra taking into account Coulomb interaction and 2 meV broadening. (b) DOLP spectra. Right panel: schematic presentation of QD in an inverted pyramid with electric contact and wavefunctions iso-surfaces of the GS CB state and parts of two lowest VB states that overlap with GS CB: green – electron; red – HH; blue - LH.

PeerJ **Chemistry Journals**

Analytical, Inorganic, Organic, Physical, Materials Science
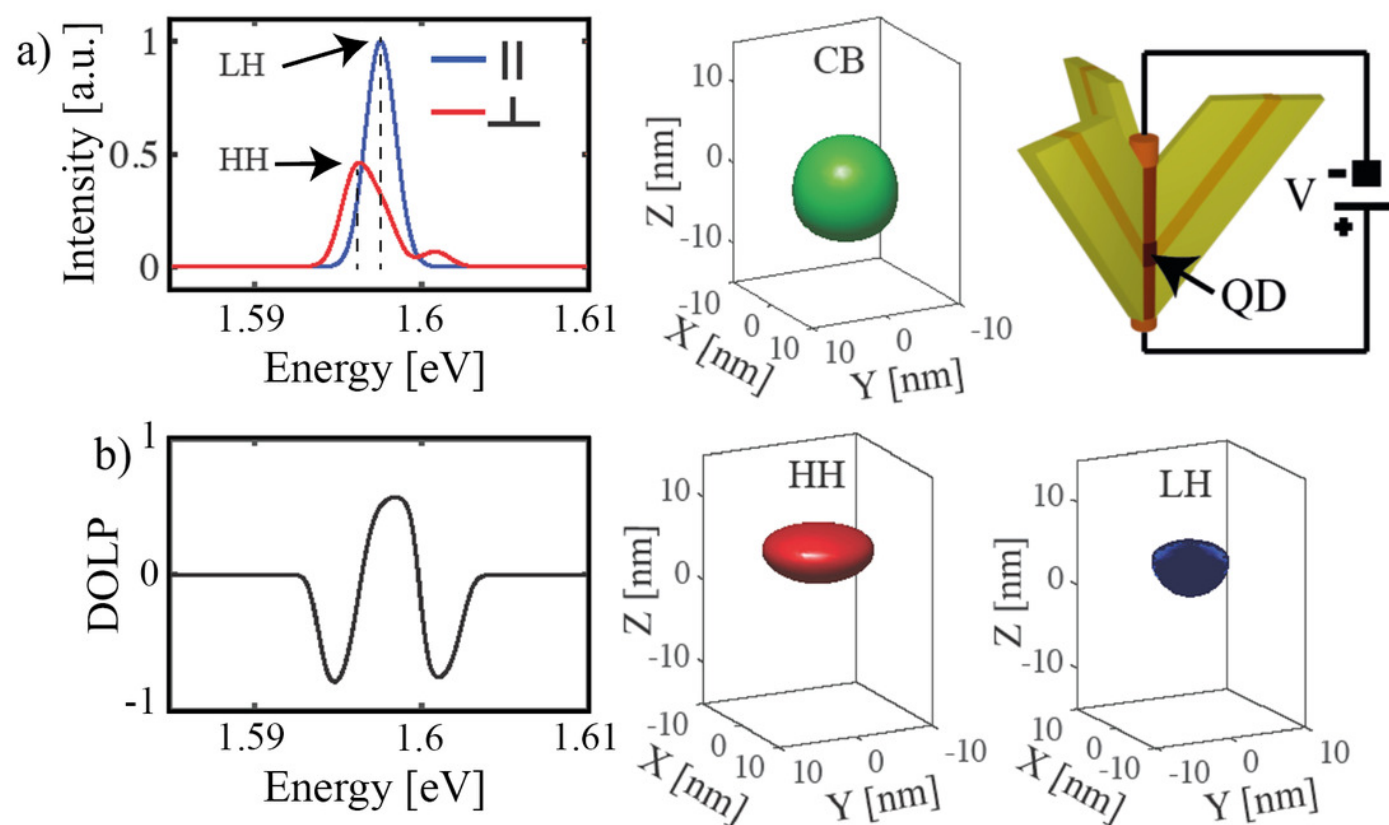
Figure 5

Schematic illustration of two QDs system (QD molecule) embedded in an inverted pyramid. The color illustrates the Al mole fraction in the different parties of the heterostructures.
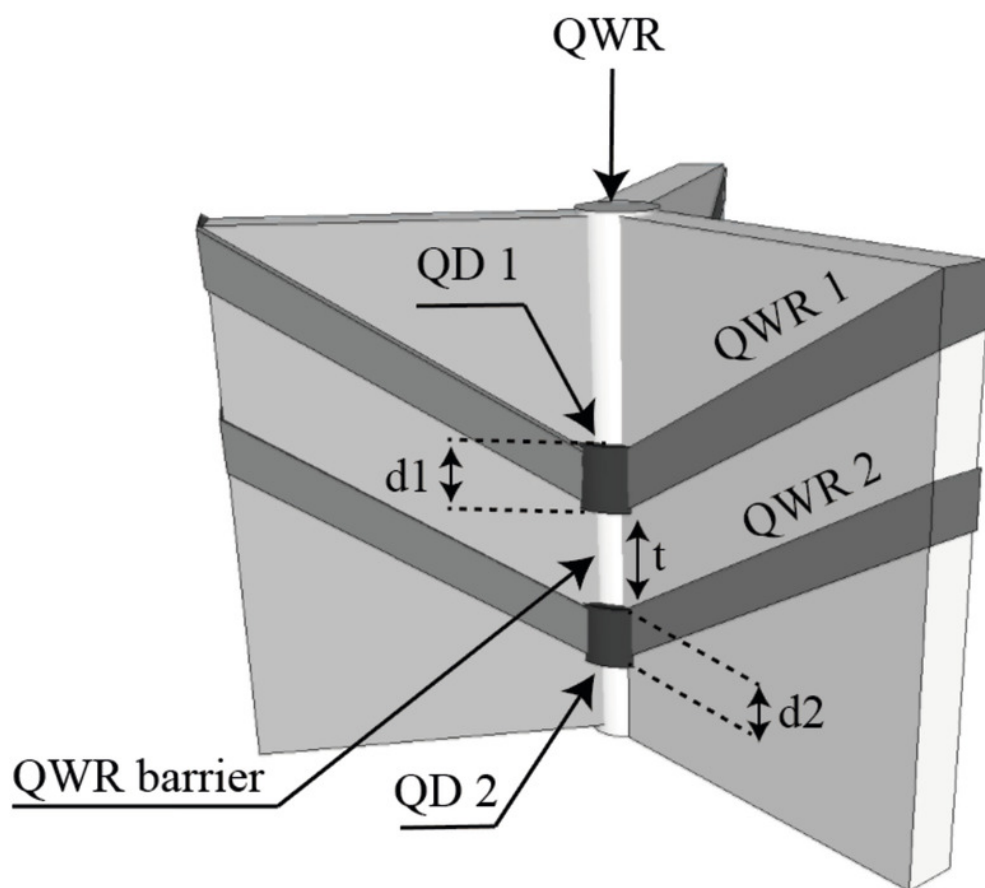
Figure 6

QDM CB and VB states control by barrier adjustment

(a) Calculated energy dependence of the first CB state versus the QDM barrier composition (in 'nominal' values of Al content). (b) Calculated energy of the first two VB states from QD barrier composition. The blue line corresponds to LH transition, red to HH transition. The inset is a schematic of the QDM core part.
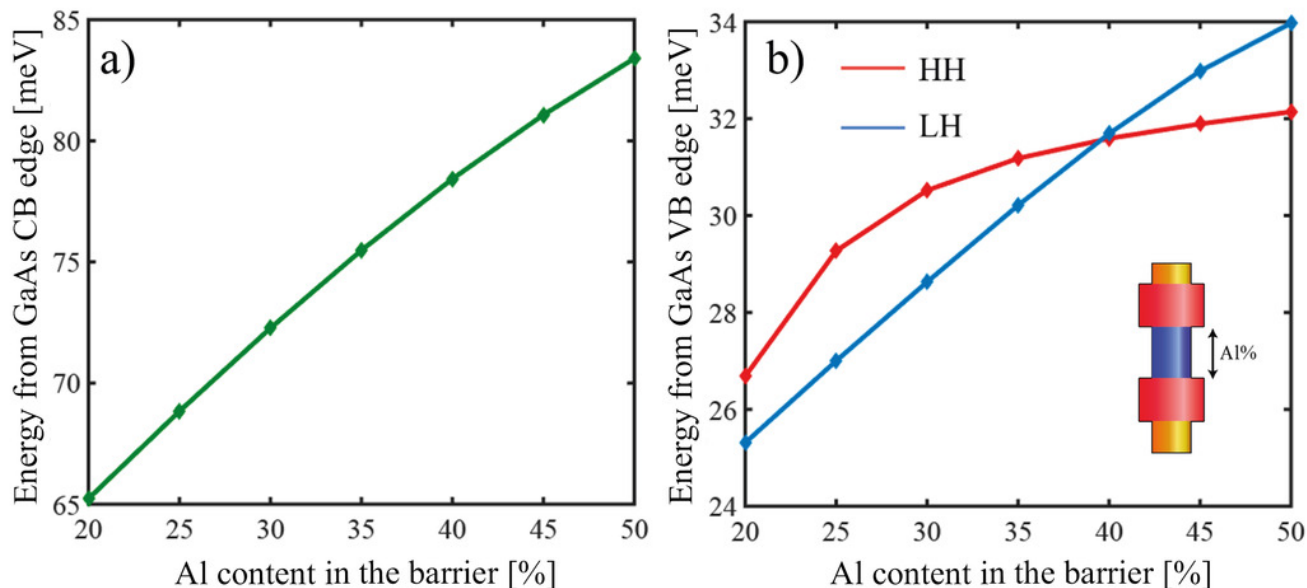
Figure 7

QDM spectra study dependence from the barrier

(a) Calculated absorption spectra of the QDM for different heights of the barrier (in 'nominal' values Al content). Lines corresponding to HH-like and LH-like transitions are indicated. (b) Calculated energies of the lowest energy transitions (a) versus QDM thickness barrier height. Different colors correspond to different transition types, the red line between CB and HH transition blue line between CB and LH transition. (c) Major wavefunction parts of the first two VB states dependence, HH - red and LH - blue.
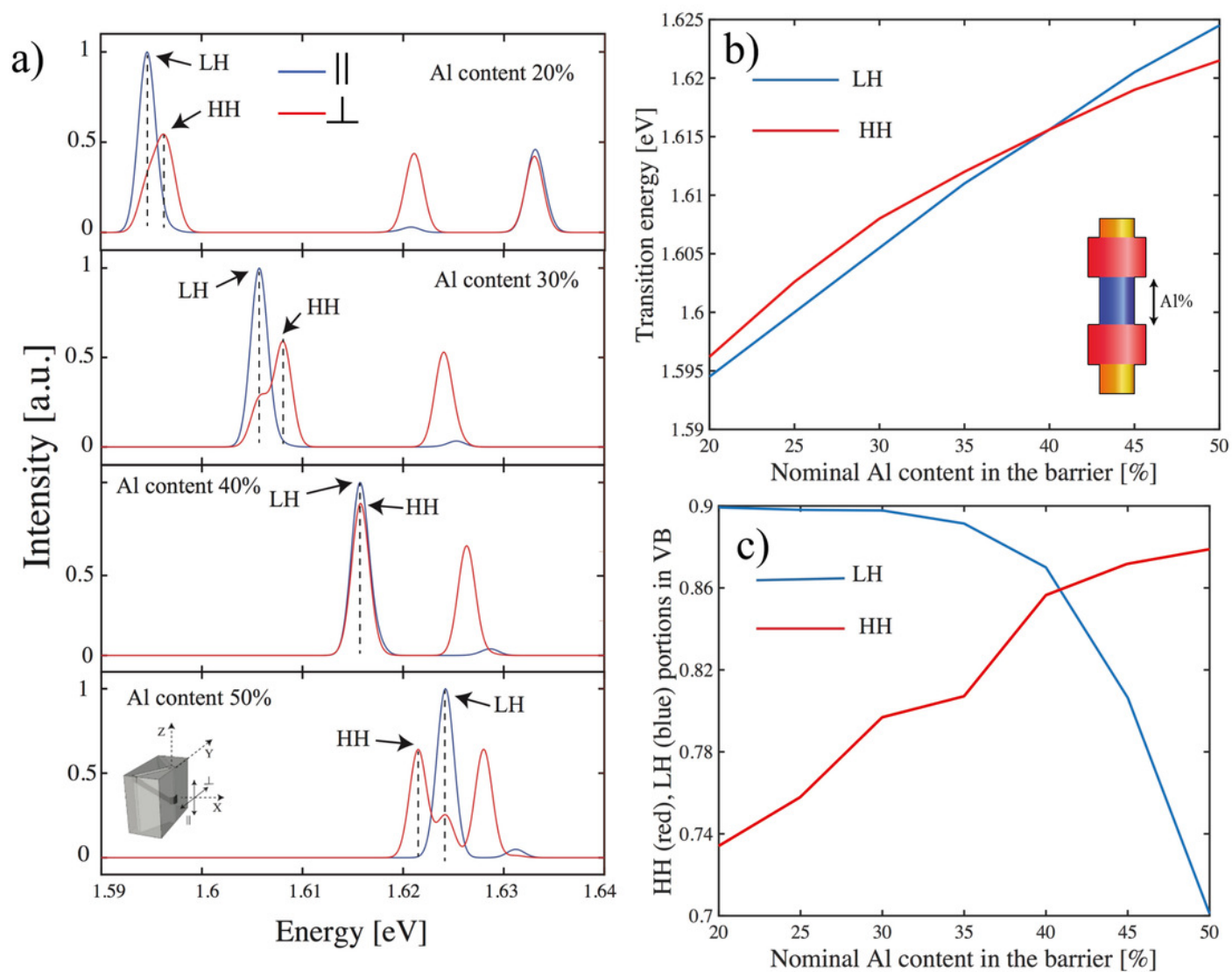
Figure 8

QDM structure nominal 35% Al content in the barriers

QDM structure (see text for parameters) without an electric field. Left panel: (a) Calculated absorption spectra taking into account Coulomb interaction and 2 meV broadening. (b) DOLP spectra. Right panel: wavefunctions iso-surfaces of the GS CB state and parts of two lowest VB states that overlap with GS CB: green – electron; red – HH; blue - LH.
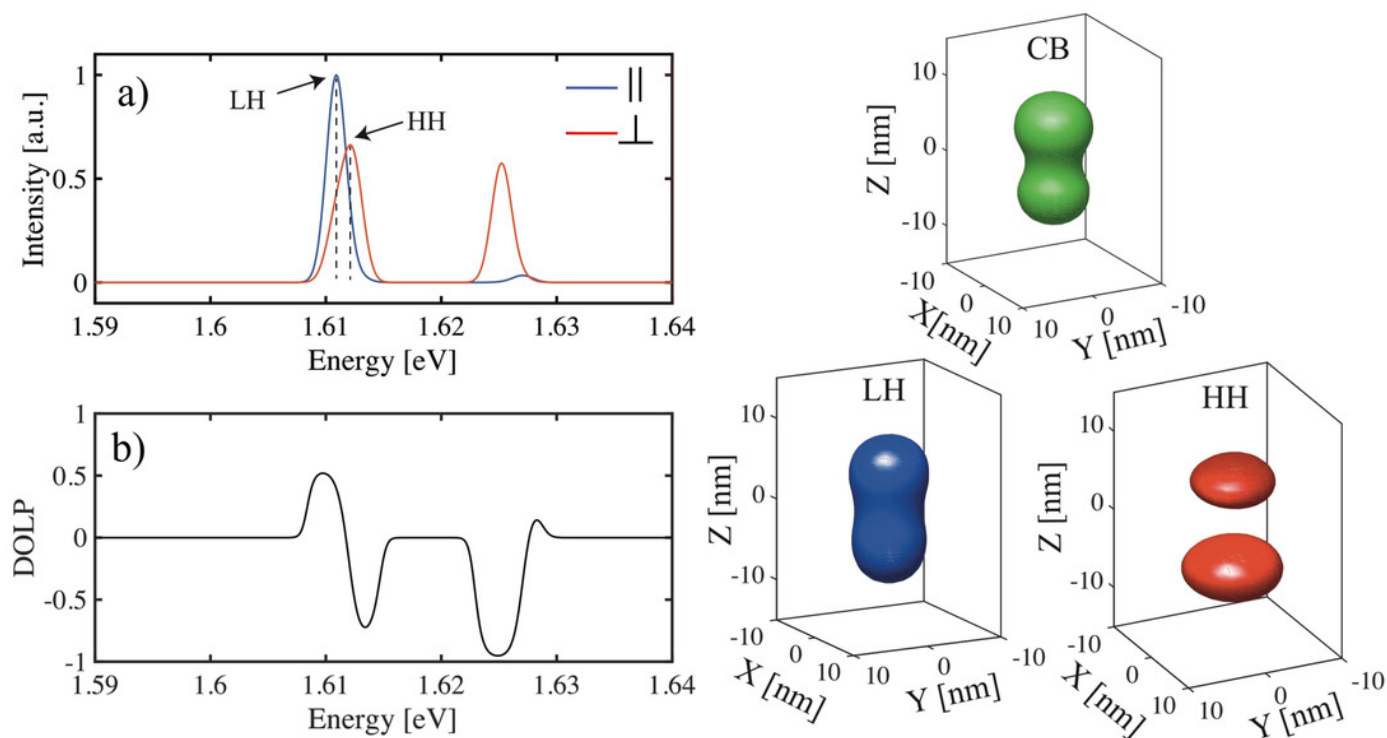
Figure 9

QDM structure subject to an electric field E=9000 V/cm

QDM structure (see text for parameters) subject to an electric field E=9000 V/cm, applied in the +z direction. Left panel: (a) Calculated absorption spectra taking into account Coulomb interaction and 2 meV broadening. (b) DOLP spectra. Right panel: wavefunctions iso-surfaces of the GS CB state and parts of two lowest VB states that overlap with GS CB: green – electron; red – HH; blue - LH.

Eigenvalues and corresponding eigenstates of the CB and VB states.

<table>
<tr><th colspan="4">Eigenvalues and corresponding eigenstates at $k=0$</th></tr>
<tr><th>Energy</th><th>First Kramers Set</th><th>Second Kramers Set</th><th>Name</th></tr>
<tr><td>E_c</td><td>$\left|\frac{1}{2},-\frac{1}{2}\right\rangle = \left|S\downarrow\right\rangle$</td><td>$\left|\frac{1}{2},\frac{1}{2}\right\rangle = \left|S\uparrow\right\rangle$</td><td>Electron</td></tr>
<tr><td>E_v'</td><td>$\left|\frac{3}{2},\frac{3}{2}\right\rangle = \frac{i}{\sqrt{2}}\left|(X+iY)\uparrow\right\rangle$</td><td>$\left|\frac{3}{2},-\frac{3}{2}\right\rangle = \frac{-i}{\sqrt{2}}\left|(X-iY)\downarrow\right\rangle$</td><td>Heavy Hole</td></tr>
<tr><td>E_v'</td><td>$\left|\frac{3}{2},\frac{1}{2}\right\rangle = \frac{-i}{\sqrt{6}}\left|(X+iY)\downarrow -2Z\uparrow\right\rangle$</td><td>$\left|\frac{3}{2},-\frac{1}{2}\right\rangle = \frac{i}{\sqrt{6}}\left|(X-iY)\uparrow +2Z\downarrow\right\rangle$</td><td>Light Hole</td></tr>
<tr><td>$E_v' - \Delta_0$</td><td>$\left|\frac{1}{2},\frac{1}{2}\right\rangle = \frac{-i}{\sqrt{3}}\left|(X+iY)\downarrow +Z\uparrow\right\rangle$</td><td>$\left|\frac{1}{2},-\frac{1}{2}\right\rangle = \frac{-i}{\sqrt{3}}\left|(X-iY)\uparrow -Z\downarrow\right\rangle$</td><td>SO Hole</td></tr>
</table>

Appendix

1 **Appendix**

2 The Hamiltonian in matrix form, considering SO interaction, looks like this: $H = H_0 + H' + H^{SO}$

3 where:

$$H_0 = \begin{pmatrix} H_1 & 0 \\ 0 & H_1 \end{pmatrix} \text{ where } H_1 = \begin{pmatrix} E_c + \varepsilon & iP_0k_x & iP_0k_y & iP_0k_z \\ -iP_0k_x & E_v + \varepsilon & 0 & 0 \\ -iP_0k_y & 0 & E_v + \varepsilon & 0 \\ -iP_0k_z & 0 & 0 & E_v + \varepsilon \end{pmatrix}$$

$$H^{SO} = \frac{\Delta_0}{3} \begin{pmatrix} 0 & 0 & 0 & 0 & 0 & 0 & 0 & 0 \\ 0 & 0 & -i & 0 & 0 & 0 & 0 & 1 \\ 0 & i & 0 & 0 & 0 & 0 & 0 & 0 \\ 0 & 0 & 0 & 0 & 0 & -1 & i & 0 \\ 0 & 0 & 0 & 0 & 0 & 0 & 0 & 0 \\ 0 & 0 & 0 & -1 & 0 & 0 & i & 0 \\ 0 & 0 & 0 & -i & 0 & -i & 0 & 0 \\ 0 & 1 & i & 0 & 0 & 0 & 0 & 0 \end{pmatrix}$$

$$H' = \begin{pmatrix} H_2 & 0 \\ 0 & H_2 \end{pmatrix} \text{ where } H_2 = \begin{pmatrix} 0 & 0 & 0 & 0 \\ 0 & L'k_x^2 + Mk_y^2 + Mk_z^2 & N'k_yk_x & N'k_zk_x \\ 0 & N'k_yk_x & Mk_x^2 + L'k_y^2 + Mk_z^2 & N'k_yk_z \\ 0 & N'k_zk_x & N'k_zk_y & Mk_x^2 + Mk_y^2 + L'k_z^2 \end{pmatrix}$$

8 A', B, L', M, N' are second order interactions due to Löwdin renormalization involving states

9 outside the S, P subspace. $\varepsilon = \dfrac{\hbar^2 k^2}{2m_0}$ and Δ_0 is the spin-orbit splitting:

10 $\Delta_0 = \dfrac{-3i\hbar}{4m_0c^2}\left\langle X \left| \dfrac{\partial V}{\partial x} p_y - \dfrac{\partial V}{\partial y} p_x \right| Y \right\rangle$. In case of GaAs, B=0.

11 This Hamiltonian contains four atomic bands, kinetic, spin-orbit, perturbation of five next bands,
12 and atomic potential in terms of mean-field. Because the transition rate is proportional to
13 $\left\langle \varphi_{cb} \left| e \cdot p \right| \varphi_{vb} \right\rangle$ where P is momentum e is a polarization vector. For optical studies, it's more
14 convenient to change the basis of this Hamiltonian to the basis of eigenfunctions of the momentum
15 operator (HH and LH basis). A set of new basis wavefunctions are presented in the following
16 Table 1 (Davies, 1997).

18 *Table 1 Eigenvalues and corresponding eigenstates of the CB and VB states.*

19 New matrix elements in this basis looks like:

$$H_0 = \begin{pmatrix}
E_c + \varepsilon & 0 & V & 0 & \sqrt{3}V^* & -\sqrt{2}U & -U & \sqrt{2}V \\
0 & E_c + \varepsilon & -\sqrt{2}U & -\sqrt{3}V & 0 & -V^* & \sqrt{2}V^* & U \\
V^* & -\sqrt{2}U^* & E_v & 0 & 0 & 0 & 0 & 0 \\
0 & -\sqrt{3}V^* & 0 & E_v & 0 & 0 & 0 & 0 \\
\sqrt{3}V^* & 0 & 0 & 0 & E_v & 0 & 0 & 0 \\
-\sqrt{2}U^* & -V & 0 & 0 & 0 & E_v & 0 & 0 \\
-U^* & \sqrt{2}V & 0 & 0 & 0 & 0 & E_v & 0 \\
\sqrt{2}V^* & U^* & 0 & 0 & 0 & 0 & 0 & E_v
\end{pmatrix}$$

$$H^{SO} = \frac{\Delta_0}{3} \begin{pmatrix}
0 & 0 & 0 & 0 & 0 & 0 & 0 & 0 \\
0 & 0 & 0 & 0 & 0 & 0 & 0 & 0 \\
0 & 0 & 1 & 0 & 0 & 0 & 0 & 0 \\
0 & 0 & 0 & 1 & 0 & 0 & 0 & 0 \\
0 & 0 & 0 & 0 & 1 & 0 & 0 & 0 \\
0 & 0 & 0 & 0 & 0 & 1 & 0 & 0 \\
0 & 0 & 0 & 0 & 0 & 0 & -2 & 0 \\
0 & 0 & 0 & 0 & 0 & 0 & 0 & -2
\end{pmatrix}$$

$$H' = \begin{pmatrix}
0 & 0 & 0 & 0 & 0 & 0 & 0 & 0 \\
0 & 0 & 0 & 0 & 0 & 0 & 0 & 0 \\
0 & 0 & -P+Q & -S^* & R & 0 & \sqrt{3/2}S & -\sqrt{2}Q \\
0 & 0 & -S & -P-Q & 0 & R & -\sqrt{2}R & \sqrt{1/2}S \\
0 & 0 & R^* & 0 & -P-Q & 0 & \sqrt{1/2}S^* & \sqrt{2}R^* \\
0 & 0 & 0 & R^* & 0 & -P+Q & \sqrt{2}Q & \sqrt{3/2}S^* \\
0 & 0 & \sqrt{3/2}S^* & -\sqrt{2}R^* & \sqrt{1/2}S & \sqrt{2}Q & -P & 0 \\
0 & 0 & -\sqrt{2}Q & \sqrt{1/2}S^* & \sqrt{2}R & \sqrt{3/2}S & 0 & -P
\end{pmatrix}$$

24   Where: $\varepsilon = \dfrac{h^2 k^2}{2m_0}$, $U = \dfrac{P_0}{\sqrt{3}} k_z$, $V = \dfrac{P_0}{\sqrt{6}}\left(k_x + ik_z\right)$, $P = \dfrac{h^2}{2m_0}\gamma_1\left(k_x^2 + k_y^2 + k_z^2\right)$,

25   $Q = \dfrac{h^2}{2m_0}\gamma_2\left(k_x^2 + k_y^2 - 2k_z^2\right)$, $S = 2\sqrt{3}\,\dfrac{h^2}{2m_0}\gamma_3\left(k_x k_z - ik_y k_z\right)$, $R = -\sqrt{3}\,\dfrac{h^2}{2m_0}\left(\gamma_2\left(k_x^2 - k_y^2\right) - 2i\gamma_3 k_x k_y\right)$

26   , $\gamma_1 = -\dfrac{2}{3}\dfrac{m_0}{h^2}\left(L' + 2M\right) - 1$, $\gamma_2 = -\dfrac{1}{3}\dfrac{m_0}{h^2}\left(L' - M\right)$, $\gamma_3 = -\dfrac{1}{3}\dfrac{m_0}{h^2}N'$.

27   Where Δ is spin-orbit splitting and $\gamma_1, \gamma_2, \gamma_3$ is Luttinger parameters (J. M. Luttinger and W.

28   Kohn, 1955). In the case of GaAs $\gamma_1 = 6.98$ $\gamma_2 = 2.06$ $\gamma_3 = 2.93$ (Vurgaftman, Meyer & Ram-

29   Mohan, 2001). In constant media, Luttinger parameters do not depend on coordinates. In the GaAs

30   media case, effective masses of light and heavy holes depend on the direction of hole propagation.

31   In case of Al$_x$Ga$_{1-x}$As Luttinger parameters are chosen as a linear interpolation between the GaAs

32   and AlAs. In AlAs, Luttinger parameters $\gamma_1 = 3.76$, $\gamma_2 = 0.82$, $\gamma_3 = 1.42$.

33   The Luttinger Hamiltonian we discussed so far is written in the x, y, and z directions corresponding

34   to the principal crystallographic directions [hhe]. We consider structures with modulated potential

35   along the z [111] direction. Thus, the Hamiltonian needs to be rewritten to a new basis. Since SO

36   and CB bands are far from LH and HH for simplicity, and we decouple them. Thus, the 3D

37   Schrodinger equation with effective mass for conduction band electrons can be solved separately

38   from Luttinger Hamiltonian for VB. The Luttinger Hamiltonian, in a new basis, looks like

39   (Fishman, 1995):

40
$$H = \begin{pmatrix} D_{HH} & -S & R & 0 \\ -S^* & D_{LH} & 0 & R \\ R^* & 0 & D_{LH} & S \\ 0 & R^* & S^* & D_{HH} \end{pmatrix}$$

41   Where

$$D_{HH} = -\frac{h}{2m_e}\left[\frac{\partial}{\partial x}(\gamma_1+\gamma_3)\frac{\partial}{\partial x} + \frac{\partial}{\partial y}(\gamma_1+\gamma_3)\frac{\partial}{\partial y} + \frac{\partial}{\partial z}(\gamma_1-2\gamma_3)\frac{\partial}{\partial z}\right] + V$$

$$D_{LH} = -\frac{h}{2m_e}\left[\frac{\partial}{\partial x}(\gamma_1-\gamma_3)\frac{\partial}{\partial x} + \frac{\partial}{\partial y}(\gamma_1-\gamma_3)\frac{\partial}{\partial y} + \frac{\partial}{\partial z}(\gamma_1+2\gamma_3)\frac{\partial}{\partial z}\right] + V$$

$$R = \frac{h}{2m_e}\sqrt{3}\left[\frac{\partial}{\partial x}\left(\frac{2\gamma_3+\gamma_2}{3}\right)\frac{\partial}{\partial x} - \frac{\partial}{\partial y}\left(\frac{2\gamma_3+\gamma_2}{3}\right)\frac{\partial}{\partial y} - i\frac{\partial}{\partial x}\left(\frac{2\gamma_3+\gamma_2}{3}\right)\frac{\partial}{\partial y} - i\frac{\partial}{\partial y}\left(\frac{2\gamma_3+\gamma_2}{3}\right)\frac{\partial}{\partial x}\right] +$$

$$+ \frac{h}{m_e}\frac{2}{\sqrt{6}}\left[\frac{\partial}{\partial x}(\gamma_3-\gamma_2)\frac{\partial}{\partial z} + \frac{\partial}{\partial z}(\gamma_3-\gamma_2)\frac{\partial}{\partial x} + i\frac{\partial}{\partial y}(\gamma_3-\gamma_2)\frac{\partial}{\partial z} + i\frac{\partial}{\partial z}(\gamma_3-\gamma_2)\frac{\partial}{\partial y}\right]$$

$$S = -\frac{h}{2m_e}\sqrt{3}\left[\frac{\partial}{\partial x}\left(\frac{\gamma_3+2\gamma_2}{3}\right)\frac{\partial}{\partial z} + \frac{\partial}{\partial z}\left(\frac{\gamma_3+2\gamma_2}{3}\right)\frac{\partial}{\partial x} - i\frac{\partial}{\partial y}\left(\frac{\gamma_3+2\gamma_2}{3}\right)\frac{\partial}{\partial z} - i\frac{\partial}{\partial z}\left(\frac{\gamma_3+2\gamma_2}{3}\right)\frac{\partial}{\partial y}\right] -$$

$$- \frac{h}{2m_e}\sqrt{\frac{2}{3}}\left[\frac{\partial}{\partial x}(\gamma_3-\gamma_2)\frac{\partial}{\partial x} - \frac{\partial}{\partial y}(\gamma_3-\gamma_2)\frac{\partial}{\partial y} + i\frac{\partial}{\partial x}(\gamma_3-\gamma_2)\frac{\partial}{\partial y} + i\frac{\partial}{\partial y}(\gamma_3-\gamma_2)\frac{\partial}{\partial x}\right]$$

42

43
44
45 **References**
46
47

48 Davies JH. 1997. *The Physics of Low-Dimensional Semiconductors*. Cambridge University
49   Press. DOI: 10.1017/CBO9780511819070.
50 Fishman G. 1995. Hole subbands in strained quantum-well semiconductors in [hhk] directions.
51   *Phys. Rev. B* 52. DOI: 10.1103/PhysRevB.52.11132.
52 J. M. Luttinger and W. Kohn. 1955. Motion of Electrons and Holes in Perturbed Periodic Fields.
53   *Physical Reviewl* 97. DOI: 10.1103/PhysRev.97.869.
54 Vurgaftman I, Meyer JR, Ram-Mohan LR. 2001. Band parameters for III-V compound
55   semiconductors and their alloys. *Journal of Applied Physics* 89:5815–5875. DOI:
56   10.1063/1.1368156.
57